

Local Structure of a Pure Bi A Site Polar Perovskite Revealed by Pair Distribution Function Analysis and Reverse Monte Carlo Modeling: Correlated Off-Axis Displacements in a Rhombohedral Material

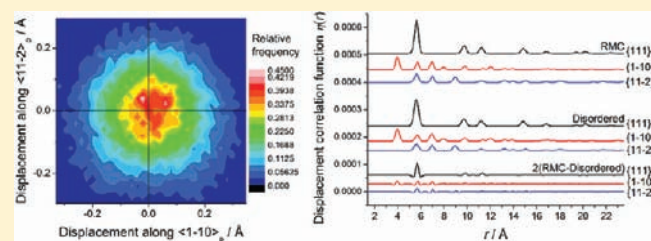
Samantha Y. Chong,[†] Robert J. Szczecinski,[†] Craig A. Bridges,[†] Matthew G. Tucker,[‡] John B. Claridge,^{*†} and Matthew J. Rosseinsky^{*†}

[†]Department of Chemistry, University of Liverpool, Liverpool L69 7ZD, U.K.

[‡]ISIS Facility, Rutherford Appleton Laboratory, Harwell, Didcot OX11 0DE, U.K.

Supporting Information

ABSTRACT: Perovskite oxides with Bi³⁺ on the A site are of interest as candidate replacements for lead-based piezoelectric ceramics. Current understanding of the chemical factors permitting the synthesis of ambient-pressure-stable perovskite oxides with Bi³⁺ on the A site is limited to information derived from average structures. The local structure of the lead-free ferroelectric perovskite Bi(Ti_{3/8}Fe_{2/8}Mg_{3/8})O₃ is studied by reverse Monte Carlo (RMC) modeling of neutron scattering data. The resultant model is consistent with the structure derived from diffraction but reveals key extra structural features due to correlated local displacements that are inaccessible from the average unit cell. The resulting structural picture emphasizes the need to combine symmetry-averaged long-range and local analysis of the structures of compositionally complex, substitutionally disordered functional materials. Local correlation of the off-axis displacements of the A site cation produces monoclinic domains consistent with the existence of displacement directions other than R ($\langle 111 \rangle_p$) or T ($\langle 100 \rangle_p$). The Bi displacements are correlated ferroelectrically both in the polar direction and orthogonal to it, providing evidence of the presence of monoclinic domains. The octahedral cation environments reveal distinct differences in the coordination geometry of the different B site metal ions. The local nature of these deviations and correlations makes them inaccessible to long-range averaged techniques. The resulting local structure information provides a new understanding of the stability of pure Bi³⁺ A site perovskite oxides.



INTRODUCTION

The search for Pb-free replacements of the ubiquitous piezoelectric actuator material PZT [the perovskite PbTi_{0.6}Zr_{0.4}O₃ at the morphotropic phase boundary (MPB) composition] is important because of regulatory pressure but challenging because of the superb figures-of-merit of PZT.^{1,2} Bi³⁺ is an alternative cation to Pb²⁺ for use on the A site of the perovskite, but it is difficult to stabilize the highly charged, distorted (due to the 6s² pair) cation on the A site of the perovskite except under pressure.^{3–12} BiFeO₃ was the only known ambient-pressure-stable example for many years. We have demonstrated that combinations of 2+, 3+, and 4+ cations on the B site can allow the stabilization of pure Bi³⁺ A site perovskites at ambient pressure.^{13,14} The material Bi(Ti_{3/8}Fe_{2/8}Mg_{3/8})O₃ is polar with a refined average structure¹⁴ (Figure 1) similar to that of BiFeO₃,¹⁵ but cation displacements away from the rhombohedral axis ($\langle 111 \rangle$ in the parent cubic perovskite unit cell) and low-symmetry microstrain both indicate that the simple R3c (R) model of BiFeO₃ is not applicable, with refinement in the monoclinic space group Cc giving an equivalent fit to the diffraction data. There are two specific points from the average structure that require local structure information for resolution: the extent to which the Bi³⁺ displacements away from the $\langle 111 \rangle$ direction (the direction of A

site displacements in BiFeO₃) are correlated between neighboring sites, which would differentiate between rhombohedral and monoclinic symmetry, and the role of the three distinct B site cations in stabilizing this pure Bi³⁺ A site material at ambient pressure. To understand how the pure Bi A site materials are stabilized, it is important to obtain complementary local structure information where short-range correlated displacements, which are averaged to zero by the symmetry operators of the average unit cell of the crystallographic structure, are evident. This “average unit cell” structure is particularly uninformative in heavily site- and composition-disordered substitutional systems (e.g., it is not possible to distinguish the average environments of the three B site cations despite their different chemistry). The average structure also assumes uncorrelated motion of individual atoms, represented by the Debye–Waller factor. In functional materials where correlated displacements are important for function, the identification of locally coupled displacements of atoms (e.g., those individually capable of contributing to polarization in this case) is essential for understanding the resulting properties. This paper reports a local structure study of Bi(Ti_{3/8}Fe_{2/8}Mg_{3/8})O₃

Received: November 14, 2011

Published: February 22, 2012

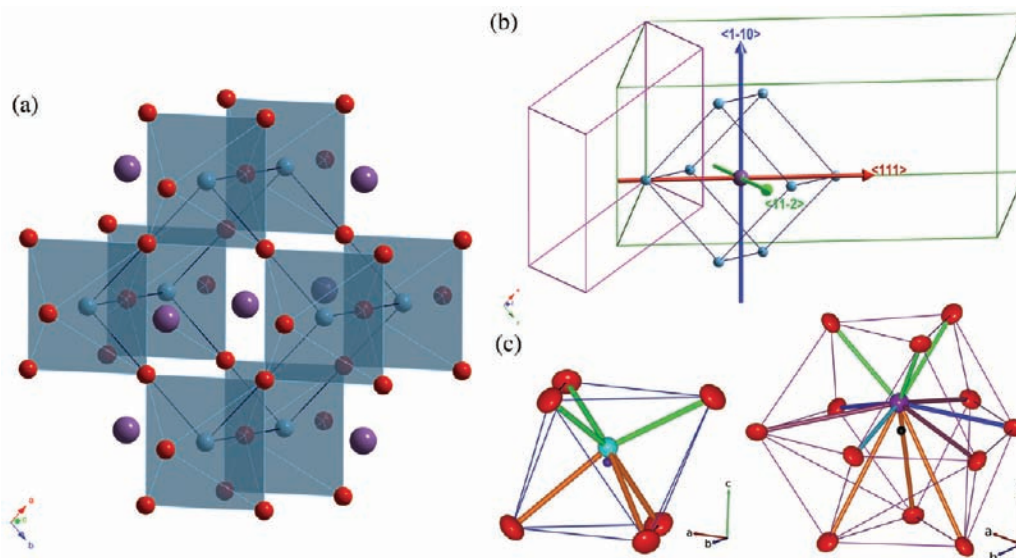


Figure 1. (a) Representation of $\text{Bi}(\text{Ti}_{3/8}\text{Fe}_{2/8}\text{Mg}_{3/8})\text{O}_3$ (Bi; purple; disordered B cation sites, light-blue; O, red) with the cubic perovskite subcell indicated. (b) Pseudocubic (dark-blue), rhombohedral R3c (green), and monoclinic Cc (magenta) unit cells with orthogonal model directions (arrows) and the corresponding pseudocubic directions indicated. (c) (left) Octahedral B cation coordination (oxygen centroid indicated as the purple sphere); (right) 12-coordinate Bi^{3+} cation environment (centroid indicated as the black sphere) from the crystallographic R3c structure¹⁰ with dominant cation displacements parallel to the pseudocubic $\langle 111 \rangle_p$ polar axis. For A and B cations, displacement along $\langle 111 \rangle_p$ results in three long bonds (orange) and three short (green) bonds to oxygen (see Table 1), and the small disordered off-axis displacement of Bi^{3+} forms a fourth short Bi–O bond (cyan). The five remaining Bi–O bonds fall into two groups (purple, dark-blue) of intermediate distance.

using total scattering methods, which reveals chemical factors controlling the stability and function that are inaccessible from the average structure.

Total scattering techniques exploit the information contained in both the Bragg and diffuse scattering, allowing a material to be characterized in terms of its long-range time-averaged structure and the local deviations from that model on a bond-length scale.¹⁶ To ensure sufficient real-space resolution, total scattering data is collected over a wide range of reciprocal-space scattering vectors Q , and the resultant data sets are corrected to account for the effects of background scattering, absorption, multiple scattering within the sample, beam intensity variations, and inelasticity (using the Placzek inelasticity correction).¹⁷ This affords the experimental total scattering structure factor $F(Q)$ and the total radial distribution function $G(r)$,¹⁸ which are related by the following Fourier transforms:

$$F(Q) = \rho_0 \int_0^\infty 4\pi r^2 G(r) \frac{\sin Qr}{Qr} dr \quad (1)$$

$$G(r) = \frac{1}{(2\pi)^3 \rho_0} \int_0^\infty 4\pi Q^2 F(Q) \frac{\sin Qr}{Qr} dQ \quad (2)$$

where $\rho_0 = N/V$ is the average number density (in atoms \AA^{-3}). $G(r)$ consists of contributions from partial radial distribution functions $g_{ij}(r)$:

$$G(r) = \sum_{i,j=1}^n c_i \bar{c}_i \bar{c}_j [g_{ij}(r) - 1] \quad (3)$$

where

$$g_{ij}(r) = \frac{n_{ij}(r)}{4\pi r^2 dr \rho_j} \quad (4)$$

in which $\rho_j = c_j \rho_0$ and $n_{ij}(r)$ is defined as the number of atoms of type j within a distance $r + dr$ of an atom of type i . The commonly used total correlation function $T(r)$ is then related to $G(r)$ by

$$T(r) = 4\pi r \rho_0 \left[G(r) + \left(\sum_{i=1}^n c_i \bar{b}_i \right)^2 \right] \quad (5)$$

The implementation of the reverse Monte Carlo (RMC) technique in the program *RMCPProfile*^{19,20} has been used previously to investigate the local structure of several perovskite materials^{21–24} and a number of Bi-containing oxides.^{25–28} Large atomistic models are refined to produce configurations that simultaneously satisfy the experimental reciprocal-space total scattering data, the real-space correlation function, and the Bragg profile data. Explicit use of the Bragg profile provides a constraint that maintains the long-range average crystal structure while instantaneous local deviations are incorporated to generate a “snapshot” of a feasible configuration consistent with all of the experimental data provided. Further details of *RMCPProfile* are available in refs 19 and 20.

RMCPProfile provides a number of constraints to incorporate additional information about the structure. In this study, two different regimes were tested: distance window constraints were used to specify the minimum and maximum distances allowed between two neighboring atom types,²⁰ while soft bond valence sum (BVS) constraints²⁹ were employed to provide information about the bonding requirements of atoms, both reducing the introduction of unphysical features during the RMC refinement and incorporating additional information to differentiate cations occupying a shared crystallographic site. The

comparison function was consequently modified to include a BVS restraint for each atom type i :

$$\chi_{\text{BVS},i}^2 = \sum_{j=1}^{N_i} (V_j - V_i)^2 / \sigma_V^2 \quad (6)$$

where N_i is the number of atoms of type i , V_j is the calculated BVS for atom j of type i , and V_i is the expected value of the BVS for atom type i .

Instantaneous bond length distributions can be extracted directly from the position and width of peaks in the resultant partial pair correlation functions $g_{ij}(r)$. Information about the neighbor frequency can be extracted from peak areas: short-range cation order would cause differences in the frequency of neighbors from the statistical distribution. This can be quantified more explicitly using the derived “near-neighbor” function $n_{ij}(r)$ ²¹ defined in eq 4, which represents the average number of atoms of type j within a sphere of radius r surrounding a central atom of type i . Comparison of the plateau values in $n_{ij}(r)$ with those expected for a random distribution indicates whether ordering is present in the RMC configuration.

METHODS

The sample of $\text{Bi}(\text{Ti}_{3/8}\text{Fe}_{2/8}\text{Mg}_{3/8})\text{O}_3$ was prepared via solid-state reaction using the previously published synthetic procedure.¹⁴ The d_{33} value of a poled ceramic was 0.6 pC/N (0 pC/N was measured before poling). Time-of-flight (TOF) neutron powder diffraction data were collected on the GEM instrument at the ISIS facility located at Rutherford Appleton Laboratory. Data were collected on ~5 g of the sample contained in an 8 mm diameter vanadium can for 900 μA h over the range $0.3 \leq Q \leq 50 \text{ \AA}^{-1}$.

Total scattering data were normalized and corrected using standard methods in the *GUDRUN*³⁰ software. The experimental $F(Q)$ was extracted using the *ATLAS* suite of programs³¹ and subsequently transformed to the total correlation function $T(r)$ using the *stog* utility in *RMCPProfile* with $Q_{\text{max}} = 30 \text{ \AA}^{-1}$, which was selected to maximize resolution while minimizing termination ripples. The real-space resolution was 0.13 \AA . The comparison in Figure 2 shows that these data are able to resolve differences in local structure between competing models. Rietveld refinement of the TOF data from the backscatter bank of the GEM instrument was carried out in *GSAS*³² [Figure S1 in the Supporting Information (SI)] using a monoclinic Cc model with cell parameters related to the rhombohedral $R3c$ structure³³ (eq S1 in the SI).

RMC refinements were performed with *RMCPProfile* using configurations consisting of a $6 \times 11 \times 11$ supercell of the monoclinic model containing 14 520 atoms, with cell edges of ~56 \AA . Refinements were constrained by fitting of the experimental total scattering structure factor $F(Q)$, the real-space correlation function $T(r)$, and the Bragg profile. The total scattering data were convoluted with a box function to account for the broadening in the calculated data due to the finite RMC configuration size,³⁴ and fits were carried out for $Q < 30 \text{ \AA}^{-1}$ (corresponding to a real-space resolution $\Delta r \approx 3.791/Q_{\text{max}} = 0.13 \text{ \AA}$). The real-space data $T(r)$ were fit over the range of the RMC configuration with $r < 23.5 \text{ \AA}$, corresponding to the shortest lattice vector. RMC refinements were run using maximum translation limits of 0.05 \AA for all of the cations and 0.1 \AA for the oxygen atoms. Initial refinements also allowed swap moves of the three octahedral cations with a probability of 0.2 of the total RMC moves. As no evidence of B site cation ordering emerged from analysis of the partial B – B pair correlation and near-neighbor functions, all subsequent refinements used static randomized B site cation distributions, for which fits of the experimental data were obtained with comparable quality to those where swapping was allowed. Refinements employed either distance window constraints on the separation of specified atom pairs or BVS

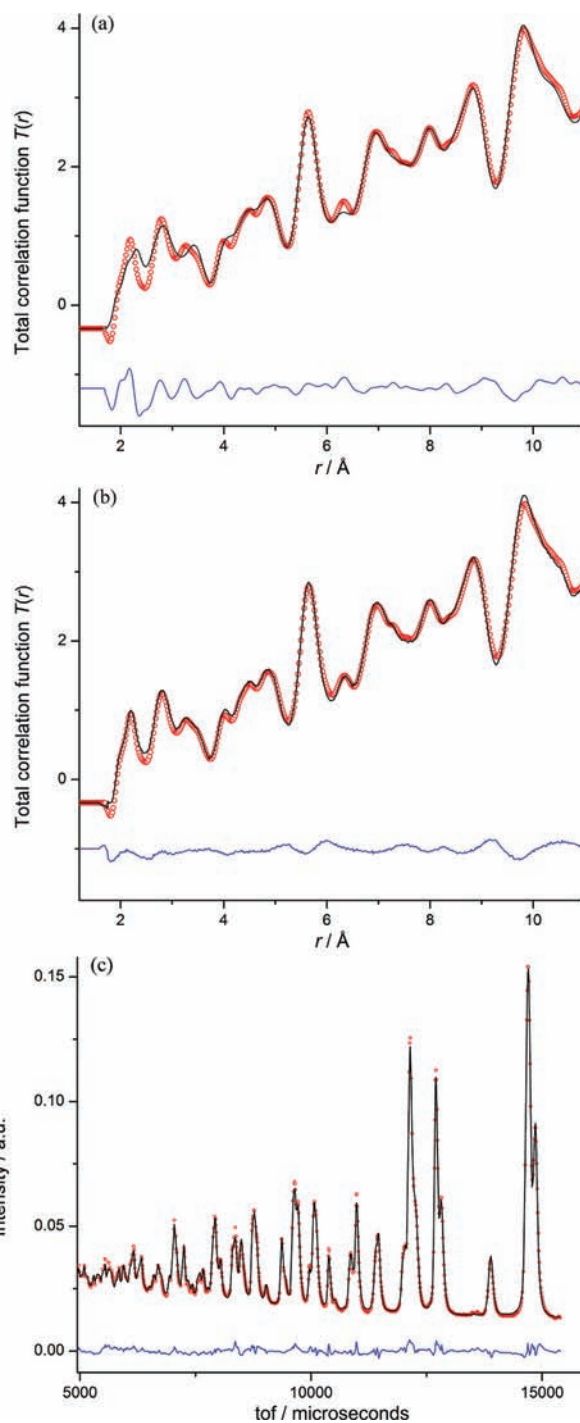


Figure 2. Total scattering data for $\text{Bi}(\text{Ti}_{3/8}\text{Fe}_{2/8}\text{Mg}_{3/8})\text{O}_3$ was collected at 298 K on the GEM instrument at ISIS over the range $0.3 \leq Q \leq 50 \text{ \AA}^{-1}$. The total correlation function $T(r)$ was generated from the Fourier transform of the total scattering structure factor $F(Q)$ with $Q_{\text{max}} = 30 \text{ \AA}^{-1}$. (a) Comparison of experimental (red \circ) and simulated (black line) total correlation functions $T(r)$ for the rhombohedral $R3c$ Rietveld model shown in Figure 1 shows that the main difference (blue line) appears at small r , indicating local deviation from the average structure at the bond length scale. RMC refinements of a $6 \times 11 \times 11$ supercell of the monoclinic model with randomized B site cation distribution using *RMCPProfile* were constrained by simultaneously fitting $T(r)$ with $r < 23.5 \text{ \AA}$, $F(Q)$ convoluted with the configuration width, and the Bragg scattering. Additional chemical information was provided using a bond valence sum (BVS) restraint to produce the fits typified here for (b) the RMC fit of $T(r)$, showing improved agreement particularly at low r , and (c) the RMC Bragg fit.

Table 1. Comparison of Bond Lengths r_{M-O} ($M = \text{Bi}^{3+}$, Ti^{4+} , Fe^{3+} , Mg^{2+}) and Octahedral Angles θ_{O-B-O} and θ_{B-O-B} in the Long-Range Average Rhombohedral Crystal Structure and Those Derived from $g_{M-O}(r)$ (Figure 6, Figure S5) and Bond Angle Distributions (Figure S4) in RMC Configurations

M	Average rhombohedral structure			Local model from RMC refinement		
	$r_{M-O}/\text{\AA}$	$\theta_{O-B-O}/\text{deg}$	$\theta_{B-O-B}/\text{deg}$	$r_{M-O}/\text{\AA}$	$\theta_{O-B-O}/\text{deg}$	$\theta_{B-O-B}/\text{deg}$
Bi^{3+}	2.242(3),					
	2.282(2),					
	2.369(4),					
	2.440(5),					
	2.598(3),					
	2.604(3),			2.26, 2.59,		
	3.156(3),			3.32 (0.4:0.6:1) ^a		
	3.161(2),					
	3.319(5),					
	3.401(3),					
Ti^{4+}		3 x 80.5(1),		1.82, 2.11	88.9, 180.5	163.9
Fe^{3+}	3 x 1.960(2),	3 x 99.9(1),		2.03	88.7, 177.6	157.1
	3 x 2.111(3),	89.6(1),	156.1(1)			
Mg^{2+}		88.3(1),		2.05	88.4, 178	155.0
		166.1(1)				

^aApproximate ratio of separations obtained from the integrated areas of peaks in $g_{\text{Bi-O}}(r)$.

constraints for all atom types. The refinement process was allowed to continue until no improvement in the fit was observed.

Refined RMC configurations were orthogonalized to a Cartesian frame with the x axis parallel to $\langle 111 \rangle_p$, y along $\langle 1\bar{1}0 \rangle_p$, and z along $\langle 11\bar{2} \rangle_p$ (Figure 1b). The $\langle \rangle_p$ subscript indicates a direction defined with respect to the $a_p \times a_p \times a_p$ cubic perovskite subcell ($a_p \approx 4 \text{ \AA}$), where $\langle 111 \rangle_p$, $\langle 110 \rangle_p$, and $\langle 001 \rangle_p$ displacements produce R, O, and T polar phases, respectively. Analysis of the geometric parameters was subsequently based on the orthogonal models. To improve the statistical accuracy for analyses with a limited sample number, the combined final configurations of 18 separate RMC refinements were used as the basis for the construction of the collapsed unit cells, the bond angle calculations, and the analysis of cation displacements.

RESULTS AND DISCUSSION

A preliminary comparison of the total correlation function simulated from the Rietveld model and the experimental function derived from total neutron scattering (Figure 2a) showed that the most significant discrepancies between the two profiles appear at short distances ($r < 4 \text{ \AA}$), corresponding to the cation–oxygen bonding distances. In the average structure, the highly distorted Bi coordination gives rise to Bi–O bond lengths that fall in this range between 2.24 and 3.50 \AA . The first peak centered at $\sim 2.2 \text{ \AA}$ is a many-component peak, with contributions from all M–O pairs ($M = \text{Bi}$, Ti , Fe , Mg). Further complexity due to the small negative scattering length of titanium is also present, and the lack of a significant negative peak suggests similar bond lengths for Ti, Fe, and Mg with oxygen. Simple deconvolution of this first peak into the constituent M–O distances was therefore not feasible; thus, to extract further information, a modeling approach, in this case RMC refinement, was required.

RMC refinements were performed using *RMCPProfile*²⁰ as described in the previous section to give satisfactory fits to the total scattering data, Bragg profile, and total correlation function, as exemplified in Figure 2b. Initial refinements employing hard distance window constraints produced reasonable fits to the experimental functions and BVS values given in Table S1 in

the SI, but unphysical sharp features in the partial correlation functions of the B site cation (Ti, Fe, Mg)–oxygen pairs at small separations due to the hard cutoff distances were observed (Figure S2). The use of a BVS constraint²⁹ for each atom type was found to alleviate these artifacts and produced fits of comparable quality for all three experimental data sets without changing the nature of the parameters from those in the distance window-based analyses evaluated from the models in the analyses described from here onward. Characteristic features of the partial correlation functions, such as the differences in octahedral cation coordination depending on the chemical identity of the B site cation, were also conserved between the two constraint regimes. To test the impact of the restraints, RMC refinements constrained solely by the BVS restraints were carried out (Table S1). These refinements produced $g_{ij}(r)$ with poorly defined features at separations longer than bonding distances (Figure S3). The BVS-only $g_{B-O}(r)$ functions showed a sharp peak at much shorter B–O distances corresponding to the parameters used in the restraints, with a slightly broader distribution of Ti–O distances than for Fe/Mg–O. These tests confirmed that the BVS constraints alone do not produce the correlations identified in the data analysis.

Initial analysis of the total and partial pair correlation functions showed good agreement with the long-range average structure derived from diffraction data (Table 1). The partial pair correlation function $g_{\text{Bi-O}}(r)$ showed a distribution of Bi–O distances similar to that observed in the averaged crystal structure. RMC refinements that allowed exchange of the B site cations showed no significant improvement in the fits to the data, and the resultant pair correlation functions $g_{B-B}(r)$ (Figure 3a) and near-neighbor functions $n_{B-B}(r)$ (Figure 3b and Table 2) for the octahedral cations indicated a random distribution of the B site cations within the sensitivity of the fitted data, which is again consistent with the disordered B site occupancy of the Rietveld model.

Condensing the 726 unit cells in the RMC configuration onto the original monoclinic unit cell (Figure 4a) produces a

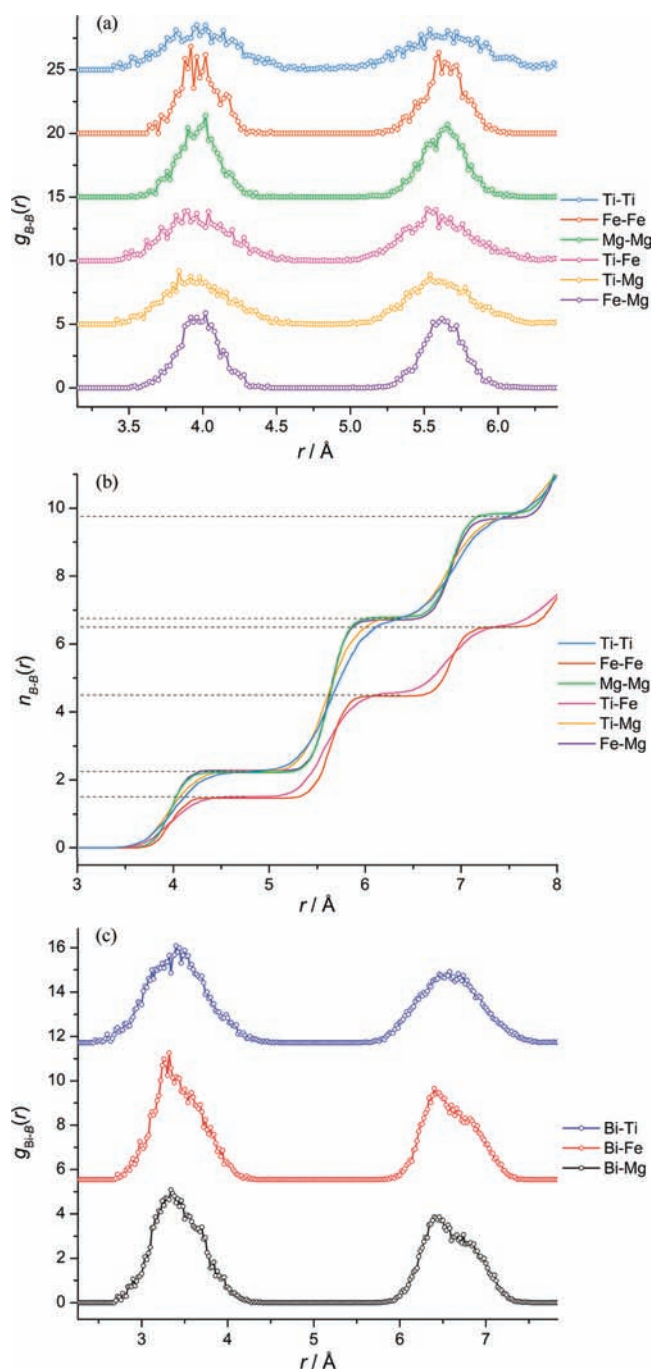


Figure 3. (a) The absence of a significant difference in peak areas between the partial pair correlation functions $g_{B-B}(r)$ indicates that there is no evidence of B site cation ordering. (b) The derived nearest-neighbor functions $n_{B-B}(r)$ show no significant difference between the neighbor frequencies and those expected for a statistically disordered distribution (dashed lines) (Table 2), confirming that ordering was not observed. (c) Pair correlation functions $g_{Bi-B}(r)$ show defined high- r shoulders for Bi–Fe and Bi–Mg, in contrast to the single broad peaks observed for Bi–Ti.

collapsed unit cell with “atom clouds” (corresponding to projections of the derived atom positions back into the parent positions in the original cell) localized close to the original crystallographic coordinates, which can be further transformed for direct comparison to the rhombohedral model (Figure 4b). This confirms that the RMC refinement maintains the long-range structure when averaged over the whole configuration and

Table 2. Nearest-Neighbor Correlations Obtained from $n_{B_1-B_2}(r)$ Functions for B Sites in the RMC Configurations

B_1-B_2	$n_{B_1-B_2}^a$					
	first shell (6 neighbors)		second shell (12 neighbors)		third shell (8 neighbors)	
	RMC	disordered	RMC	disordered	RMC	disordered
Ti–Ti	2.26	2.25	4.51	4.50	3.2	3.0
Fe–Fe	1.46	1.50	3.01	3.00	2.0	2.0
Mg–Mg	2.22	2.25	4.57	4.50	3.1	3.0
Ti–Fe	1.51	1.50	3.07	3.00	2.0	2.0
Ti–Mg	2.26	2.25	4.50	4.50	3.0	3.0
Fe–Mg	2.28	2.25	4.51	4.50	2.9	3.0

^a $n_{B_1-B_2}$ indicates the number of B_2 neighbors in the shells surrounding B_1 . The existence of short-range B site cation ordering within the sensitivity of the data would be seen as significant differences between the observed (RMC) $n_{B_1-B_2}$ values and the values calculated for statistically disordered B site cation occupancies.

allows visualization of local-length-scale detail in the displacement parameters. The general shapes of these atom clouds are consistent with those obtained from Rietveld refinement, with the oxygen atom displacement elongated in directions orthogonal to the B –O bonds. The bismuth clouds display a complex structured shape that does not have the threefold rotational symmetry expected for a rhombohedral-derived model. This may point to the coexistence of two of the monoclinic twin domains expected from symmetry lowering from rhombohedral, a possibility investigated in later analysis. This is consistent with the average structure refinement, where the Bi position differs from the simple R model through displacement away from the threefold axis.

One aspect immediately apparent from the folded supercell is the difference in the distributions of the three chemically distinct B site cations (Figure 5). This could not be tackled in the average structure refinement, where a single B site is used, giving local cation environments that do not satisfy the expected local bonding at each cation, as seen by the deviation from the expected BVS (Table S1). The Ti atoms appear as diffuse clouds, while Fe and Mg cations form more densely clustered isotropic cores at each octahedral site. These effects are evident in the B –O pair correlation functions (Figure 6) and three-body geometric functions (Figure S4 and Table S2) and are apparent in both the distance window and BVS-constrained models. The $g_{Ti-O}(r)$ has a sharp peak centered at 1.82 Å, with a broader feature at a higher r value of ~ 2.11 Å. The shorter distance of the sharp peak indicates a Ti–O bond length ~ 0.1 Å shorter than in $SrTiO_3$ ³⁵ but close to the shortest Ti–O distance in tetragonal $BaTiO_3$ (1.83 Å)³⁶ and having a breadth and shape of the distribution similar to those observed for F_R -PZT.³⁷ The longer distance indicated by the broad feature is also comparable to the longer Ti–O distances in $BaTiO_3$ (2.13 Å) and a number of monoclinic phases of PZT (2.11–2.15 Å).^{38,39} The modeled Ti–O distances thus agree well with expectations based on a range of polar perovskites containing Ti. In contrast, the partial correlation functions for Fe–O and Mg–O show a single peaks centered at 2.03 and 2.05 Å, respectively, consistent with more regular environments where the displacement is almost exclusively along $\langle 111 \rangle_p$ to form three long and three short Fe/Mg–O bonds as observed in the bulk structure (2.111 and 1.960 Å) (Table 1). The B – B cation pair correlation functions (Figure 3a) also show peaks

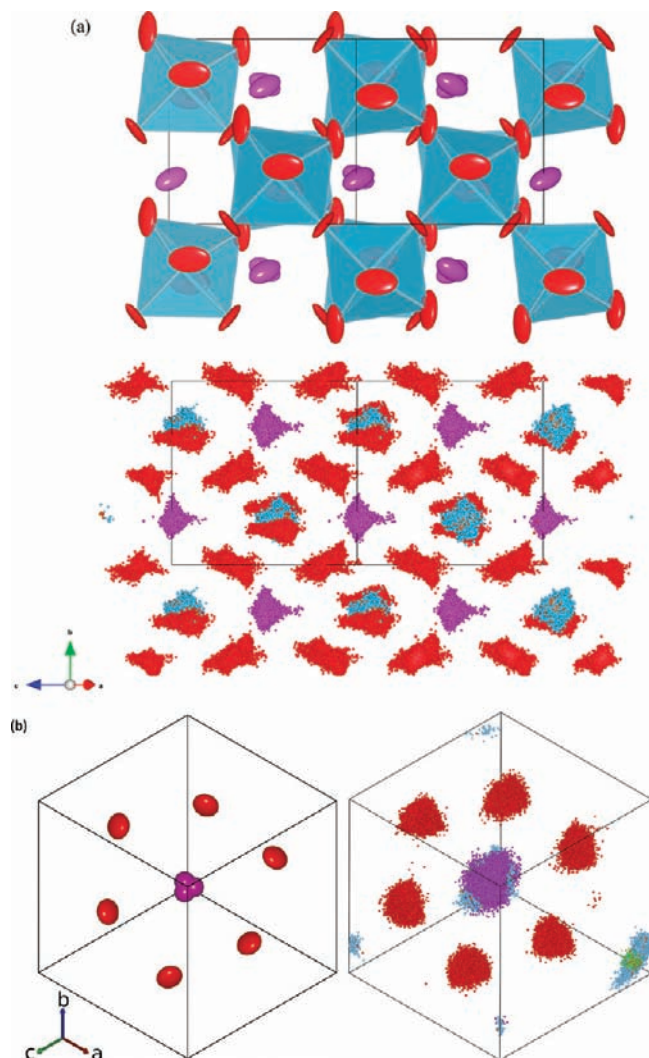


Figure 4. (a) (top) Monoclinic Cc Rietveld model viewed along $[101]$ with Bi and O atomic displacement parameter (ADP) ellipsoids and (bottom) representation of 18 RMC configurations ($6 \times 11 \times 11$ supercells of the monoclinic model, each containing 14 520 atoms) collapsed back onto the Rietveld monoclinic unit cell, showing qualitative similarities between the shapes of the ADPs and atom clouds for oxygen and a complex structure of the Bi clusters. (b) (left) Rhombohedral $R3c$ Rietveld model viewed along $(111)_p$ showing the uniform threefold positions of Bi displaced orthogonal to $\langle 111 \rangle_p$ and (right) 18 RMC configurations condensed onto the rhombohedral unit cell showing an off-axis cloud of Bi atoms without the expected threefold-symmetric distribution.

for the Ti–B pairs that are much broader than those between iron and magnesium, representing a wider variation in the separation of Ti and Fe/Mg pairs than between combinations of Fe and Mg. The bond angle distributions show a similar effect: while average bond angles within and between octahedra agree closely with those derived from Rietveld analysis, the distribution of angles is markedly broader for the Ti^{4+} sites (Figure S4 and Table S2). In local structure experimental and computational studies of PZT,^{40–42} octahedral Ti is found to be more active in off-center displacement than Zr, which is essentially undisplaced.

These contrasts in octahedral cation coordination are further highlighted by differences in the displacement of B site cations from the oxygen centroid (Table 3), which together with the Bi

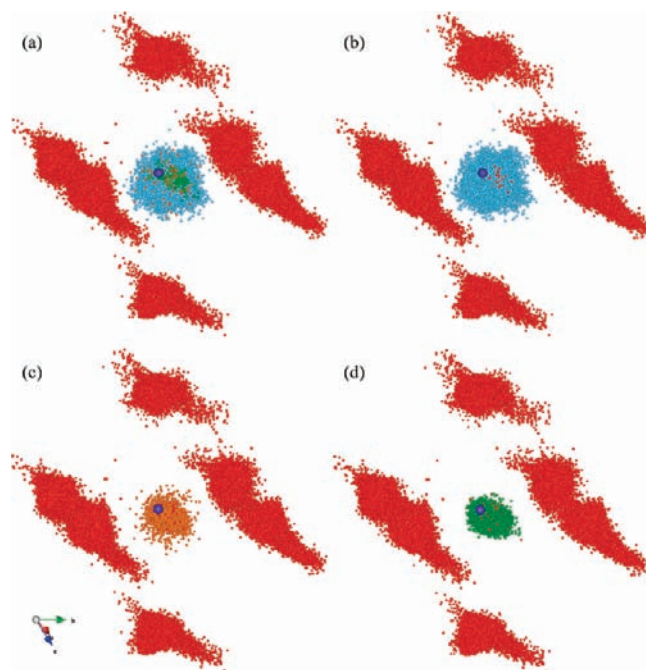


Figure 5. RMC configurations condensed onto the original rhombohedral cell, centered on the B site and viewed close to $[\bar{1}01]$, showing distribution clouds for (a) all of the octahedral cations and (b) Ti^{4+} , (c) Fe^{3+} , and (d) Mg^{2+} cations (oxygen centroids are shown as purple spheres).

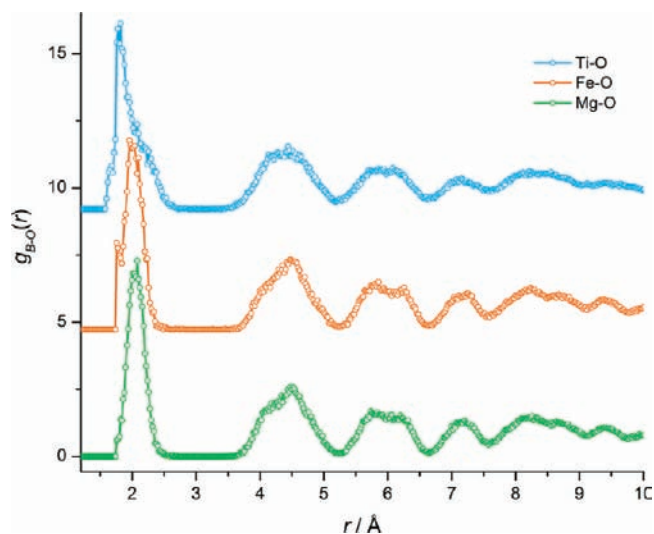


Figure 6. Partial $g_{B-O}(r)$ correlation function for B site cation–O pairs. Ti shows a distinctive distribution with a sharp peak centered at $r \approx 1.82$ Å and a broad shoulder at $r \approx 2.11$ Å. In contrast, the Fe–O and Mg–O distributions are relatively sharp and symmetric, centered at 2.03 and 2.05 Å, respectively.

centroid displacements determine the overall polarization. The distribution of the total average displacements (Figure 7a) again shows that Ti^{4+} has a broader range of displacements, demonstrated by the broad asymmetric peak centered at 0.31 Å with a full width at half-maximum (fwhm) of 0.36 Å, which is markedly different from the displacements observed for iron (0.26 Å) and magnesium (0.27 Å) cations and also much greater than the average value for the single $R3c$ Rietveld model B site (0.24 Å). The larger mean displacement for Ti is consistent with its role in determining the ferroelectric structures of

Table 3. Octahedral B Site Displacements from the Centroid of Coordinated O Atoms (d) Obtained from the Distributions in Figure 7a–d, Along with fwhm Values of the Fitted Peaks (w)^a

direction	Ti ⁴⁺		Fe ³⁺		Mg ²⁺	
	$d/\text{\AA}$	$w/\text{\AA}$	$d/\text{\AA}$	$w/\text{\AA}$	$d/\text{\AA}$	$w/\text{\AA}$
Total absolute displacement	0.312(2) ^b	0.355(6)	0.259(2)	0.274(8)	0.267(1)	0.264(4)
$\langle 111 \rangle_p$	0.131(3)	0.456(9)	0.239(5) ^b	0.317(3)	0.242(7) ^b	0.315(3)
$\langle 1\bar{1}0 \rangle_p$	-0.003(3)	0.62(1)	-0.004(1)	0.209(3)	0.0009(6)	0.219(2)
$\langle 11\bar{2} \rangle_p$	-0.007(1)	0.279(4)	-0.033(1)	0.203(3)	-0.033(1)	0.239(4)

^aPeaks were fitted with Gaussian distributions, unless otherwise noted. ^bPeak was fitted with an asymmetric function.

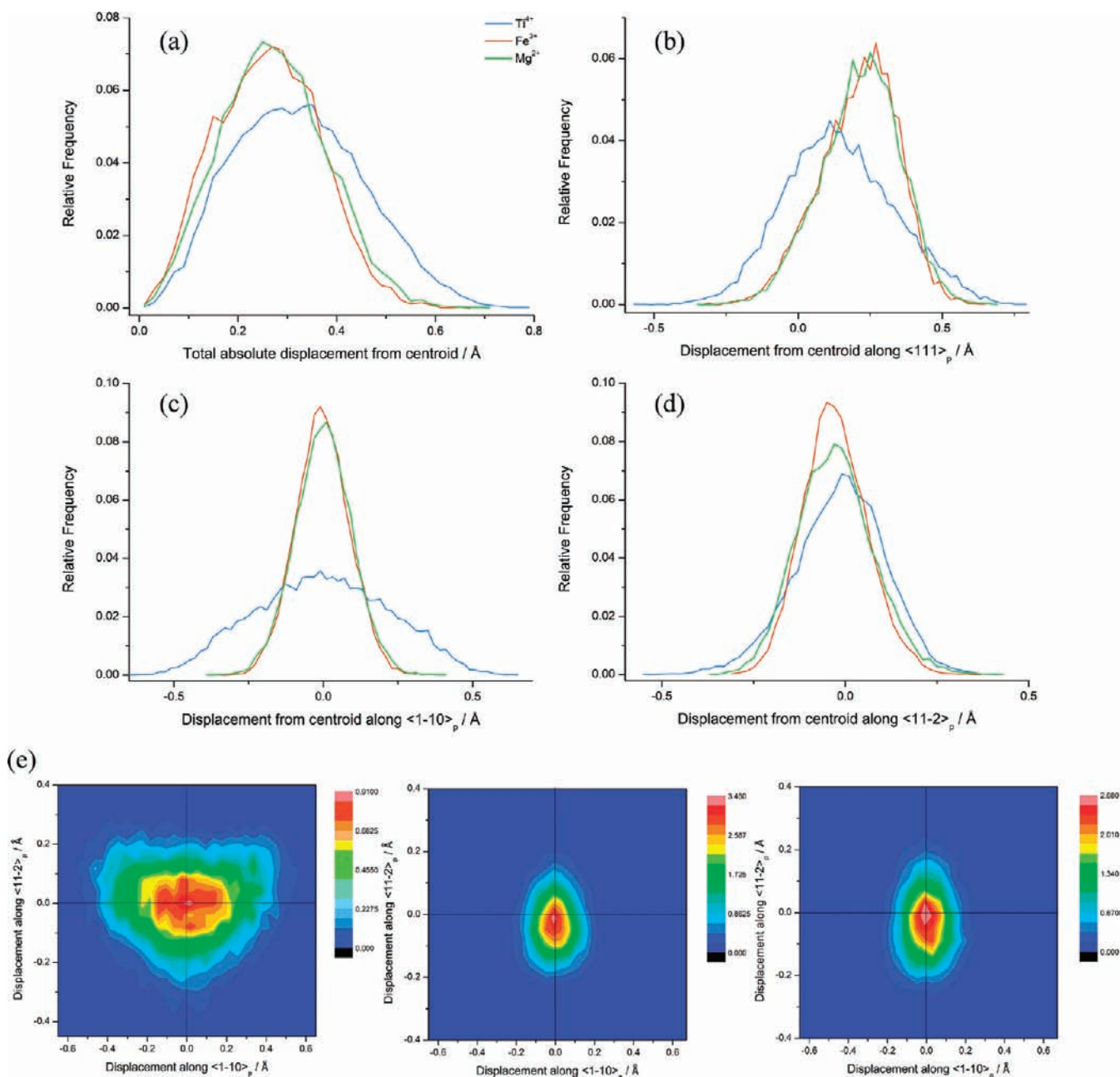


Figure 7. Distribution of (a) total B site cation displacement and (b–d) displacements from the oxygen centroid along (b) $\langle 111 \rangle_p$, (c) $\langle 1\bar{1}0 \rangle_p$, and (d) $\langle 11\bar{2} \rangle_p$. (e) Density plots corresponding to a view down $\langle 111 \rangle_p$ of the off-axis B site cation displacements along $\langle 11\bar{2} \rangle_p$ and $\langle 1\bar{1}0 \rangle_p$, showing (left) a broad distribution for Ti⁴⁺ in contrast to narrower, more uniform displacements for (center) Fe³⁺ and (right) Mg²⁺.

a range of materials. The distinctive behavior of the Ti cation was investigated more closely by examining the separate components of B site cation displacement along the orthogonal

Cartesian directions, defined to include the $\langle 111 \rangle_p$ and $\langle 1\bar{1}0 \rangle_p$ directions, which are important in ferroelectric perovskites (Figure 7b–d). The dominant displacement direction for all

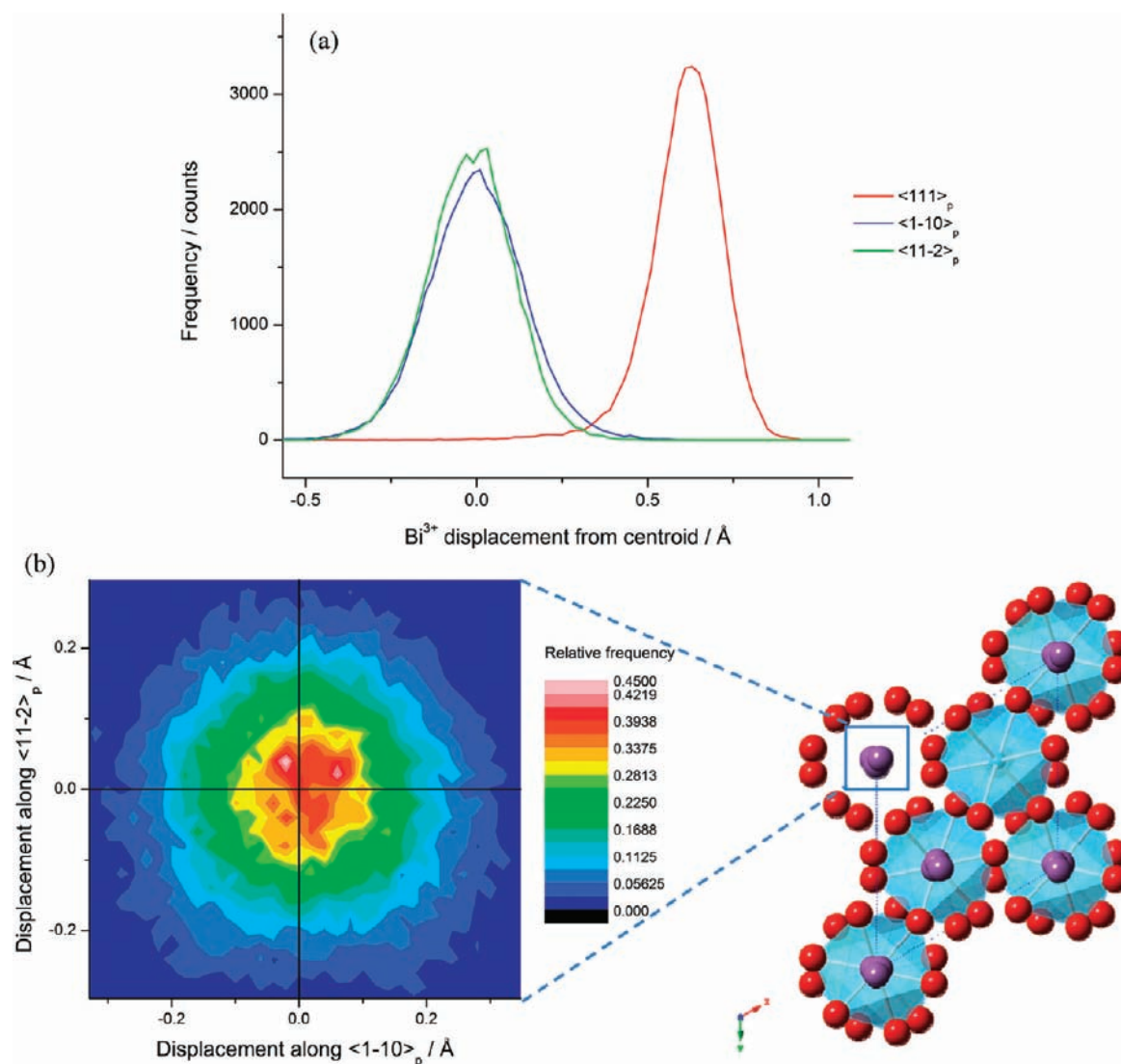


Figure 8. (a) Distribution of Bi displacements along the Cartesian model directions in the pseudocubic cell as defined in Figure 1, showing a large displacement along the polar axis and no significant mean orthogonal vector over the length scale of the RMC configuration. (b) Density plot of the off-axis components corresponding to a view along $\langle 111 \rangle_p$ centered on the Bi site, showing two peaks (pale pink) away from the origin indicating that on a local scale, there are two main populations of Bi cations displaced normal to the polar axis.

three octahedral cations is along the bulk polar axis $\langle 111 \rangle_p$, with similar asymmetric distributions centered at 0.24 Å observed for Fe and Mg. However, the peak for Ti^{4+} displacement along the polar axis indicates a much smaller average displacement of 0.13 Å, which is more symmetrical and significantly broader, with a fwhm of 0.46 Å compared with 0.32 Å for Fe and Mg. The distribution of $\langle 111 \rangle_p$ displacements for Ti contains negative displacements (i.e., displacements opposite to the domain polarity), which are not found for the other B site cations. This shows that for Ti, the majority of the mean displacement is not along $\langle 111 \rangle_p$ but along other directions. Orthogonal to $\langle 111 \rangle_p$, small displacements of -0.03 Å are observed along $\langle 11\bar{2} \rangle_p$ for Fe^{3+} and Mg^{2+} . Again, the displacement of Ti^{4+} differs, with an average off-axis displacement close to zero and a broader distribution. This contrast in variability of the Ti cation is most noticeable in the displacement along $\langle 1\bar{1}0 \rangle_p$. The mean displacement of all three B cations along $\langle 1\bar{1}0 \rangle_p$ is small, but the extremely broad Ti peak (fwhm 0.62 Å) represents a wide distribution of Ti^{4+} positions that average to approximately zero over the scale of the RMC configuration. The distribution of

the combined B site displacements orthogonal to $\langle 111 \rangle_p$ (Figure 7e) highlights the fact that the most frequent displacements are close to zero, but for Ti, this incorporates a wide range of values. This shows that there are extensive positive and negative displacements along the $\langle 1\bar{1}0 \rangle_p$ direction, which is the Ti displacement direction found in the O phase of BaTiO_3 .³⁶ Ti has the largest off-centroid mean displacement of all three B site cations, but these displacements are the least concentrated along $\langle 111 \rangle_p$, with the most significant frequency of displacements being against the dominant direction. The local correlation of these displacements is not revealed by this form of analysis of the data but would be expected to be important for the functional behavior of the material.

The local environment of the A site bismuth cation is also modeled well by the long-range Rietveld structure. The distribution of Bi–O distances (Figure S5) shows approximate pair separations and proportions similar to those predicted by the average structure (Table 1). The partial Bi–B pair correlation functions (Figure 3c) show similar distributions of Fe–Bi and Mg–Bi separations with a defined shoulder toward high r

Table 4. Bi³⁺ Displacements from the Centroid of Coordinated O Atoms (*d*) Obtained by Peak Fitting of the Displacement Distributions in Figure 8a, Along with fwhm Values of the Fitted Peaks (*w*);^a

direction	Bi ³⁺	
	<i>d</i> /Å	<i>w</i> /Å
total absolute displacement	0.659(1) ^b	0.213(5)
$\langle 111 \rangle_p$	0.630(1) ^b	0.219(2)
$\langle 1\bar{1}0 \rangle_p$	-0.0007(4)	0.317(1) ^c
$\langle 11\bar{2} \rangle_p$	-0.0152(7)	0.289(2) ^c

^aPeaks were fitted with Gaussian distributions, unless otherwise noted. ^bPeak was fitted with an asymmetric function. ^cBreadth of the off-axis displacement distributions arises from their bimodal nature, accounting for the small mean values.

on the peaks in $g_{\text{Bi-Fe/Mg}}(r)$. However, $g_{\text{Bi-Ti}}(r)$ does not have these features, appearing instead as broadened single peaks, consistent with its varied displacements. As a simple assessment of the possible effect of *B* site cation neighbors on the Bi coordination environment, as suggested for Ti-rich regions in PZT,⁴⁰ bismuth sites were considered as distinct types dependent on the number of Ti neighbors in the first surrounding *B* site shell. The distribution of Bi–O distances was largely unchanged as a function of Ti⁴⁺ neighbors (Figure S6 and Table S3) suggesting that the type of surrounding *B* site cation does not have a significant effect on Bi–O coordination. The mean displacement of Bi³⁺ cations from the centroid of the oxygen cage is 0.64(9) Å, which is close to that observed for the Rietveld model (0.66 Å). The main component of the displacement is parallel to the $\langle 111 \rangle_p$ polar direction of the average structure (Figure 8a) with all of the Bi cations moving in the same sense, confirming that the RMC model retains the ferroelectricity throughout the length scale of the configuration, with the simulation box corresponding to a single polar *R3c* domain (i.e., when judged on the sense of displacement along $\langle 111 \rangle_p$). Rietveld refinement in the rhombohedral *R3c* space group required a 0.11 Å displacement of Bi orthogonal to the polar axis away from the special position. The Bi displacement distributions orthogonal to $\langle 111 \rangle_p$ (Figure 8a and Table 4) are broader than the polar displacement and average to approximately zero because of Bi displacements of both polarities along $\langle 1\bar{1}0 \rangle_p$ and $\langle 11\bar{2} \rangle_p$, which correspond to a bimodal distribution of displacements. A mean absolute off-axis displacement of 0.17(9) Å that is approximately equal in the two directions [0.11(9) and 0.10(8) Å for $\langle 1\bar{1}0 \rangle_p$ and $\langle 11\bar{2} \rangle_p$, respectively] is observed in the RMC configuration with a distribution that shows two dominant peaks of density (Figure 8b) rather than the threefold pattern associated with a purely rhombohedral symmetry. Representations of the local structure can be derived using the most frequently occurring Bi displacement, the modal *B* site cation positions, and the crystallographically averaged oxygen coordinates (Figure 9 and Figure S7). This unit cell incorporates the small off-axis cation displacements without the imposition of an assumed symmetry on the local structure. This representation of the structure emphasizes the displacement of the Bi off the threefold axis and the distinct behavior of the *B* site cations. The use of the mode position to represent Ti does not reflect the range of displacements found along $\langle 1\bar{1}0 \rangle_p$.

The average *R* structure treats all of the off-axis displacements of the *A* site cation as uncorrelated, but the PDF analysis does not require this constraint on the structural description. Pair displacement correlation functions (DCFs) $\eta(r)$ between

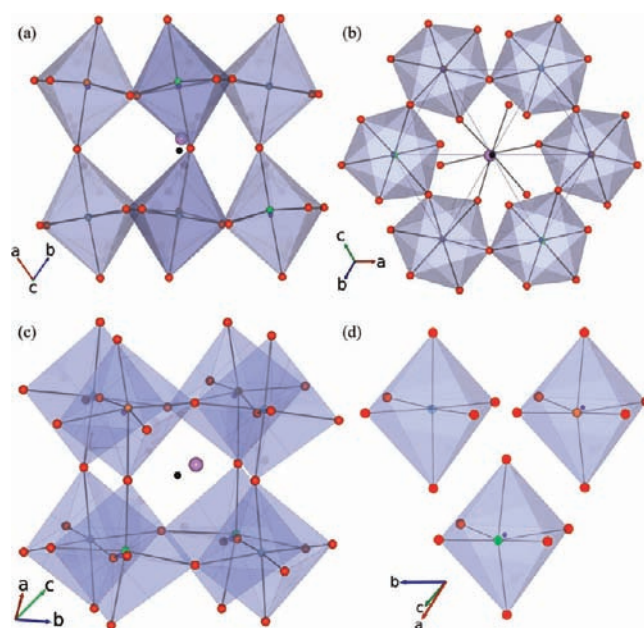


Figure 9. Representation of the local unit cell structure in which the Bi position (purple) was determined from the mode value of the displacements in the RMC configurations with a positive component along $\langle 1\bar{1}0 \rangle_p$ (corresponding to the dense regions at the right in Figure 8b) and the *B* site cation positions (Ti, blue; Fe, orange; Mg, green) were calculated from their overall mode displacements from the coordinated oxygen centroid (shown in black for Bi and purple for the *B* site). (a–c) Views (a) along $\langle 110 \rangle_p$, (b) along $\langle 111 \rangle_p$, and (c) close to $\langle 11\bar{2} \rangle_p$ are displayed. Local displacements orthogonal to $\langle 111 \rangle_p$ are shown to be correlated by analysis of the displacement correlation function (Figure 10b), confirming the local monoclinic symmetry. (d) View centering on the local *B* site octahedral coordination that shows the similarity of the Fe and Mg displacements, mainly along $\langle 111 \rangle_p$, while the mode Ti position lies close the centroid despite its broad distribution of displacements (Figure 7).

two types of cation can be calculated for the RMC configuration:^{23,24}

$$\eta(r) = \frac{1}{Nr^2} \sum \mathbf{u}_i \cdot \mathbf{u}_j \quad (7)$$

where \mathbf{u}_i is the vector describing the displacement of cation *i* and *r* is the separation between the pair of cations whose displacements are being considered. In this implementation, the displacement of each cation from the centroid of its coordinated oxygen atoms was calculated, and the DCF was obtained by summing over the volume of the configuration for all specified cation pairs *i* and *j*. The inherent contribution due to the underlying crystallographic periodicity was discarded by subtracting a “background” DCF generated from a disordered configuration in which the arrangement of cation displacements had been randomized by exchanging the centroid displacements statistically between the cation sites. This removed correlations due to the symmetry of the average structure. Specifically, the resultant differential DCF represents correlations distinct from those expected on the basis of the polar nature of Bi-(Ti_{3/8}Fe_{2/8}Mg_{3/8})O₃. As the total displacement vector \mathbf{u} is dominated by the component in the polar direction $\langle 111 \rangle_p$, it was necessary to separate the DCF into the components along the Cartesian axes related to the perovskite subcell to investigate the correlation of more subtle features, such as off-polar-axis displacements.

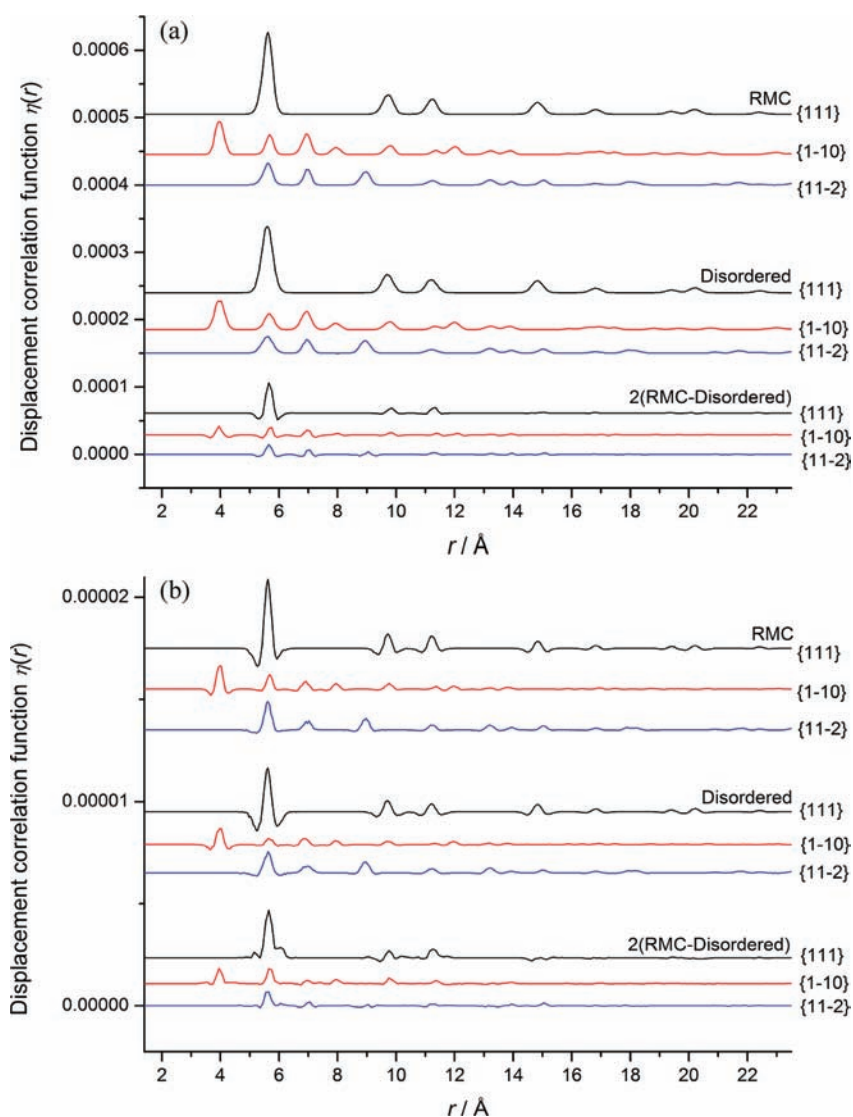


Figure 10. Bi–Bi pair displacement correlation functions (DCFs) calculated for (a) displacements parallel to the polar axis $\langle 111 \rangle_p$ and (b) off-axis displacements with summed components along $\langle 1\bar{1}0 \rangle_p$ and $\langle 11\bar{2} \rangle_p$ and visualized as correlations within planes normal to those directions. In both cases, the DCFs were calculated for the RMC configuration (top) and a configuration with a randomly disordered displacement distribution (middle) to generate a differential DCF (bottom) representing correlations distinct from those due to the underlying periodicity. Positive peaks are observed for displacements both parallel and normal to the polar direction, indicating that both polar and orthogonal displacements are correlated over the range of $r = 10\text{--}15 \text{ \AA}$.

For $\eta_{\text{Bi-Bi}}(r)$ (Figure 10), these correlations were further resolved into three separate planes within the structure that are orthogonal to the directions considered in order to visualize the correlations between Bi atoms within these planes. The DCFs calculated for Bi pairs in both the RMC and disordered configurations show large correlations of bismuth displacements parallel to the bulk polar axis (Figure 10a). Positive peaks are retained in the differential $\eta_{\text{Bi-Bi}}(r)$, indicating that the correlation between the Bi displacements along the polar direction is stronger than would be predicted for the long-range average structure. This indicates that the ferroelectric Bi displacements are correlated to the extent that the magnitude of the polar displacements influences those of the surrounding Bi cations (i.e., similarly sized Bi displacements along $\langle 111 \rangle_p$ tend to cluster together). Peaks in $\eta_{\text{Bi-Bi}}(r)$ persist to at least $r = 10\text{--}15 \text{ \AA}$, indicating that these correlations extend over a range approximately on the order of the RMC configuration box size. The DCFs calculated for vectors with components in the

$\langle 1\bar{1}0 \rangle_p$ and $\langle 11\bar{2} \rangle_p$ directions (i.e., off-polar-axis displacements) show that the displacements normal to $\langle 111 \rangle_p$ are also correlated (Figure 10b). The peaks are an order of magnitude smaller than those along $\langle 111 \rangle_p$ because of the reduced displacement in these directions, but they again extend to $r = 10\text{--}15 \text{ \AA}$, suggesting that the correlation of the small off-axis displacements persists over a range similar to those of the larger polar displacements. This confirms that displacements orthogonal to the polar axis are correlated monocrystallically on a local scale, that is, the distribution of nonzero off-axis displacements is not statistically disordered over the sample but instead is correlated into local domains where monoclinic off-axis displacements similar to those proposed ($\sim 0.2 \text{ \AA}$) for the M phase ($x = 0.48$) of PZT^{43,44} are seen. The domain size indicated by the extent of the peaks in the DCF is consistent with the presence of two or more monoclinic domains within the RMC configuration with a cell edge of $\sim 56 \text{ \AA}$. This corresponds to the two peaks of off-axis Bi density observed in Figure 8b and reflects the fact that the most

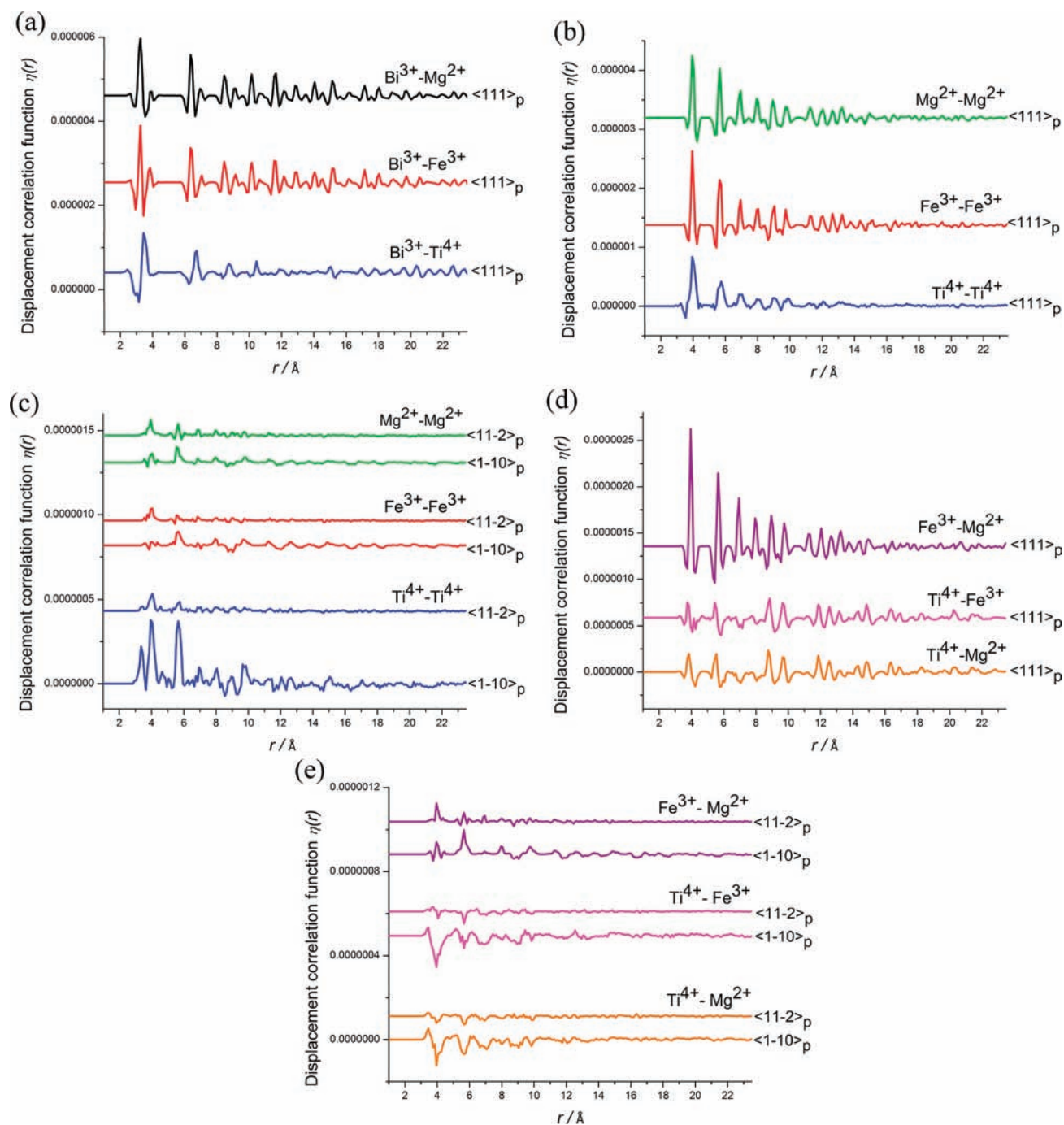


Figure 11. (a) Differential Bi–B cation pair displacement correlation functions calculated within a spherical volume along directions parallel to the polar axis $\langle 111 \rangle_p$, showing that correlations of Bi–Fe/Mg polar displacements are stronger and persist to a greater distance ($r = 15\text{--}20\text{ \AA}$) than those for Bi–Ti pairs ($r = 10\text{--}15\text{ \AA}$). (b, c) Differential B–B cation DCFs of homopairs (Mg–Mg, Fe–Fe, Ti–Ti) for (b) displacements parallel to the polar axis $\langle 111 \rangle_p$ and (c) off-axis ($\langle 1\bar{1}0 \rangle_p$ and $\langle 11\bar{2} \rangle_p$) displacements. The DCFs in (b) show weaker correlation of Ti pairs parallel to $\langle 111 \rangle_p$. However, the off-axis displacements of Ti shown in (c) are correlated to those of neighboring Ti, while those of Fe and Mg are not coupled to cation displacements of the same type. (d, e) Differential B–B DCFs of heteropairs (Fe–Mg, Ti–Fe, Ti–Mg) for (d) displacements parallel to the polar axis $\langle 111 \rangle_p$ and (e) off-axis ($\langle 1\bar{1}0 \rangle_p$ and $\langle 11\bar{2} \rangle_p$) displacements. These DCFs show that Fe–Mg displacements are correlated along $\langle 111 \rangle_p$, while those of Ti–Fe/Mg pairs are uncorrelated parallel to the polar axis and anticorrelated normal to it.

frequent Bi displacements from the O centroid are not along $\langle 111 \rangle_p$ as in the R phase³³ but include off-axis components. This locally monoclinic structure would not be apparent over the longer range of a crystallographic refinement, as the observed nanodomain size would produce symmetry averaging to R; this explains the origin of the observed anomalous microstrain broadening due to the local M symmetry. The local symmetry at

Bi does not have the threefold axis characteristic of rhombohedral symmetry.

DCFs were also evaluated for Bi–B cation pairs to examine whether the distinctive Ti^{4+} behavior extends to correlation of its displacements with those of bismuth. DCFs were again calculated for displacements parallel to $\langle 111 \rangle_p$ (Figure 11a) and perpendicular to the R polar axis (Figure S8). The positive

peaks in $\eta_{\text{Bi}-B}(r)$ for displacements along $\langle 111 \rangle_p$ show that the displacements of all three *B* site cations are correlated with those of bismuth. However, while $\eta_{\text{Bi}-\text{Fe}/\text{Mg}}(r)$ shows displacement correlations that persist beyond $r = 20 \text{ \AA}$, the length scale of the Bi–Ti correlations appears to be shorter, with significant peaks in $\eta_{\text{Bi}-\text{Ti}}(r)$ observed only to $r = 10\text{--}15 \text{ \AA}$. This is consistent with Ti being displaced significantly along other directions, reflecting its ability to adopt a range of distorted structures in octahedra in ferroelectric oxides. A further distinctive feature of $\eta_{\text{Bi}-\text{Ti}}(r)$ is the shape of the first peak at $r \approx 3.3 \text{ \AA}$, which suggests that the displacement of Bi^{3+} and Ti^{4+} separated by the shorter distances covered by this peak are anticorrelated, while those at the longer extreme of the peak are positively correlated. These anticorrelated pairs correspond to the small-*r* tail of the Bi–Ti distribution in $g_{\text{Bi}-\text{Ti}}(r)$ (Figure 5c). Considering the pattern of Ti displacements along $\langle 111 \rangle_p$, there is a significant frequency of antipolar displacements in the opposite sense to the majority along this direction within the RMC cell, and this suggests that those displacements occur when there are short Bi–Ti contacts. Displacements of Bi and *B* site cations orthogonal to the polar axis show no evidence of being correlated. Contrasts in the correlation of Ti displacements are also observed in the DCFs for *B*–*B* pairs (Figure 11b–e). While $\eta_{\text{Ti}-\text{Ti}}(r)$, $\eta_{\text{Fe}-\text{Fe}}(r)$, and $\eta_{\text{Mg}-\text{Mg}}(r)$ show that the displacements parallel to $\langle 111 \rangle_p$ are correlated for all of the homopairs, the peaks in $\eta_{\text{Ti}-\text{Ti}}(r)$ are broader and extend over a shorter distance (Figure 11b). Of the heteropair (Ti–Fe, Ti–Mg, Fe–Mg) DCFs along $\langle 111 \rangle_p$, $\eta_{\text{Fe}-\text{Mg}}(r)$ (Figure 11d) shows that the displacements of Fe–Mg pairs along the polar axis are also correlated, with a similar strength to the homopairs; near-neighbor Fe–Mg pairs have displacements correlated similarly to Fe–Fe and Mg–Mg pairs, but those of Ti–Fe/Mg pairs are not. This is consistent with frequent off-axis displacements by Ti in a manner not positively coupled to Fe and Mg cation neighbors but correlated with any local Ti neighbors [see $\eta_{\text{Ti}-\text{Ti}}(r)$]. The corresponding off-axis DCFs (Figure 11e) further confirm these differences. $\eta_{\text{Ti}-\text{Ti}}(r)$ implies that Ti displacements are correlated up to $r = 10\text{--}15 \text{ \AA}$ for $\langle 1\bar{1}0 \rangle_p$ displacements, and $\eta_{\text{Ti}-\text{Fe}/\text{Mg}}(r)$ shows that displacements of Ti and both Mg and Fe atoms are anticorrelated, with the influence also extending to $r = 10\text{--}15 \text{ \AA}$. In contrast, the DCFs calculated for pairs involving only Mg^{2+} and/or Fe^{3+} (Fe–Fe, Mg–Mg, Fe–Mg) show no correlation between those cation displacements orthogonal to $\langle 111 \rangle_p$. These correlations (reduced Ti–Bi $\langle 111 \rangle_p$ correlations and strong Ti–Ti off-axis correlations) suggest that the Ti cations may nucleate regions where the polarization is not aligned with the *R* structure direction, although the off-axis correlations between Bi and any of the *B* site cations are not pronounced (Figures S8 and S9).

Differences in the local structure of the octahedral cations were immediately noticeable from the initial pair correlation function analysis. Clearly apparent from the partial pair correlation functions was flexibility in the coordination of the Ti^{4+} cation, as evidenced by a broader distribution of separations and angles. This variability in geometry can be attributed to the availability of low-energy *d* states of the d^0 cation and its small size, enabling second-order Jahn–Teller distortion.⁴⁵ While the displacement parallel to the polar direction is coupled to that of Bi^{3+} , the correlation length of less than 15 \AA is shorter than that for Fe and Mg. Furthermore, Bi–*B* DCFs indicate little significant off-axis correlation, while the $\eta_{\text{Ti}-B}(r)$ functions clearly show coupling of the small displacements orthogonal to $\langle 111 \rangle_p$ suggesting that *B* site cations are influenced by the off-center

movement of neighboring *B* site cations rather than the Bi^{3+} . *A* site cations because of direct competition for relevant bonding with *O* neighbors. Although these correlations extend to up to 20 \AA , the effect is canceled out on the length scale of the RMC configuration. Information on these local differences and short-range correlations is not accessible by Rietveld refinement, as the detail is lost in averaging over the bulk crystal structure.

CONCLUSIONS

The Rietveld-refined crystal structure of the polar Bi^{3+} perovskite $\text{Bi}(\text{Ti}_{3/8}\text{Fe}_{2/8}\text{Mg}_{3/8})\text{O}_3$ conceals significant local structural features and short-range correlations. Previous work had shown that satisfactory Rietveld refinement of $\text{Bi}(\text{Ti}_{3/8}\text{Fe}_{2/8}\text{Mg}_{3/8})\text{O}_3$ in the polar rhombohedral space group *R3c* required a lower-symmetry microstrain model than permitted by the crystallographic symmetry and displacement of the Bi^{3+} cation orthogonal to the bulk polar axis. The crystallographic model contained a single disordered *B* site occupied by three different cations, each with distinct bonding requirements, which bond valence sums suggested were not fully satisfied by occupying a common site. Through the use of time-of-flight neutron total scattering data and RMC modeling, local deviations from the crystal structure have been extracted to account for the discrepancies in the refined crystal structure.

RMC refinement of an atomistic model constrained by the total scattering data, real-space correlation function, and Bragg scattering plus BVS or distance window constraints was used to generate several snapshots of the disordered crystalline structure. Many of the average structural parameters of the RMC configurations were remarkably well described by the Rietveld model. Mean bond distances, bond angles, and displacements were generally in close agreement with those derived from the crystal structure. No evidence for ordering of the octahedral cations was observed in refinements allowing atom swapping.

Analysis of the cation displacements orthogonal to the bulk polar $\langle 111 \rangle_p$ axis revealed local monoclinic fluctuations within the RMC model, requiring correlation between the cation displacements distinct from the simple correlation of ferroelectric displacements along the $\langle 111 \rangle_p$ direction; the off-axis displacements do not occur in an uncorrelated way associated with statistical disorder within *R* symmetry, but positive displacements occur in a locally coupled way that locally breaks the threefold axis and lowers the symmetry to monoclinic (Figure 12), as in the *Cc* cell used to give an equivalent fit to the disordered *R* cell in the original structure analysis. The length scale of these correlations indicates a monoclinic domain size of up to 15 \AA , encompassing the volume of approximately two to three *Cc* unit cells, containing clusters of up to 12 Bi atoms. The presence of locally monoclinic clusters accounts for the anomalous microstrain broadening required for Rietveld refinement of the rhombohedral model. The $\eta_{\text{Bi}-\text{Bi}}(r)$ function also suggests that Bi displacements along the $\langle 111 \rangle_p$ polar axis are correlated in both direction and magnitude up to a distance of 15 \AA , resulting in a tendency of similarly sized displacements to cluster.

The RMC model produces a local environment surrounding Ti^{4+} that contrasts with those around Fe^{3+} and Mg^{2+} , resulting in more chemically sensible environments for each cation than in the average structure. While Fe and Mg show little variation from the octahedral coordination described by the Rietveld model, Ti^{4+} demonstrates extensive flexibility in its coordination geometry, consistently resulting in broader distributions of pair separation distances and displacements. The Ti disorder may be overestimated as a result of interference between

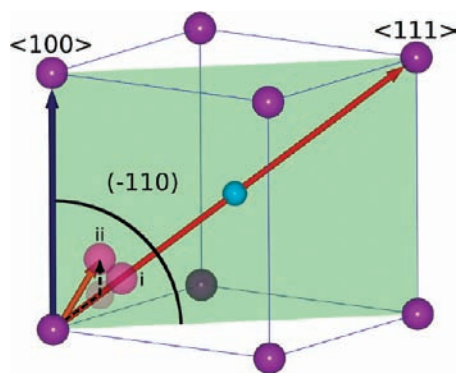


Figure 12. Schematic relating bismuth displacements to the cubic perovskite subcell directions. In F_R phases, the polarization vector (and A site displacement direction) is along $\langle 111 \rangle_p$, while in the tetragonal structure F_T it lies parallel to $\langle 100 \rangle_p$. Dominant cation displacements along $\langle 111 \rangle_p$ (i) with small disordered off-axis shifts (ii) are consistent with the F_R phase, as has been suggested for F_R -PZT.³³ Freezing-out of shifts along $\langle 100 \rangle_p$, with correlated displacements in the $(\bar{1}10)$ plane (shown in green), results in the monoclinic F_M -PZT phase proposed by Noheda et al.⁴⁴ as a phase linking the F_T and F_R phases on either side of the MPB.

negative Ti–B and positive B–B correlations in $g(r)$, in regard to which further information may be accessible through Ti-specific probes such as EXAFS. The good BVS and Rietveld agreement gives confidence in the deduced distributions, and in particular, the Ti BVS in the RMC model (both using distance window and BVS constraints) corresponds more closely to crystal chemical expectations than in the average structure, where the assumption that all three B site cations occupy the same site gives bond lengths that do not suit any of them. The correlations of Ti^{4+} displacements were found to differ from those of the other B site cations, with the coupling of polar displacements to Bi^{3+} extending over a shorter range and the correlation of off-polar-axis displacements to those of other B cations, with particularly pronounced ferroelectric Ti–Ti correlations along $\langle 1\bar{1}0 \rangle_p$. Both Ti and Bi are displaced from $\langle 111 \rangle_p$ in a locally individually correlated manner, but the off-axis Ti and Bi displacements do not appear to be significantly correlated to each other. The Fe and Mg cation displacements along $\langle 111 \rangle_p$ are similarly correlated to those of Bi, whereas B site Ti behaves differently. The ability of Ti to be displaced locally along different directions within the octahedron of nearest-neighbor O atoms, when coupled with the other B site displacement patterns observed, may play a key role in stabilizing this pure Bi A site perovskite. This is an interesting observation for future materials discovery work, as it suggests that combining predominant $\langle 111 \rangle_p$ displacements from a subset of B site cations with displacements along other directions (Ti) is an effective way to accommodate Bi on the A site of a perovskite within a polar structure. Fe displacements along $\langle 111 \rangle_p$ following Bi (and correlated by size as shown by the DCF) are expected on the basis of the structure of $BiFeO_3$ and the ability of $d^5 Fe^{3+}$ to adopt a range of coordination environments due to its absence of strong ligand-field preferences for specific environments. However, the observation of significant noncentric displacements by Mg is surprising, as such s -block cations are usually associated with more symmetrical environments, suggesting that O displacements driven by Bi produce electrostatic effects that in turn drive coupled Mg displacements. The bonding at $d^0 Ti^{4+}$ is well-known to permit a broad

range of distorted octahedral environments, and here displacements similar to those in the orthorhombic $BaTiO_3$ structure³⁶ and also onto lower-symmetry directions are seen. The lack of strong coupling between Bi and Ti displacements may impact the functional ferroelectric behavior.

The scale of local deviations from the long-range structure that we have revealed by close analysis of the RMC models are on the order of bond distances, with no B site cation ordering apparent. The displacement correlation lengths and hence the domain sizes are larger yet still within the limits of the configuration used to generate the RMC models. Information about local structure on these length scales is inaccessible by Rietveld refinement, but by the use of real-space correlation functions and RMC modeling, several unexplained aspects of earlier crystallographic studies have been resolved. The observation of nanosized domains of correlated off-axis displacements of the polarization away from the $\langle 111 \rangle_p$ axis of canonical R-structure FE perovskites has been shown to be possible, allowing rotation of the polarization away from the T and R directions toward that found in the M_A phase of PZT (Figure 12), with the ~ 0.17 Å off-axis displacements being comparable to the 0.2–0.25 Å displacement seen in the PZT M phases. This not only supports the formation of nanodomains that are averaged out in conventional diffraction studies but also shows that such domains do not need to have the polarization (and their structures) solely restricted to the well-known R and T structures. Thus, the debate between polarization-rotation and nanophase-separation models at the PZT MPB⁴⁶ should recognize that within the R and T symmetries, local correlation can persist and significantly change the structure without impacting the metric symmetries or diffraction-observed symmetry operators.^{47,48} Here we have found in a single-phase material local, correlated off-axis displacements for both the A and B sites that do not correspond to the canonical T and R structures.

The correlated displacements within the $(\bar{1}10)_p$ plane represented in Figure 12 correspond to the ordered displacements required to form the M phases. These displacements correspond to monoclinic local symmetry and suggest that the Cc structure originally considered in the analysis of the average structure is present in the nanodomains, with extra disorder due to Ti displacement along noncanonical directions: the Fe and Mg displacements are predominantly along the original R polar direction, with off-axis Bi displacements driving the formation of the M nanodomains. The Ti–Ti correlations are significantly off-axis but not strongly correlated with those of any of the other atoms, suggesting that when Ti–Ti pairs occur (which they do statistically), the interaction between the Ti–O bonds produces specific displacement patterns. Similarly Bi–Ti correlations along the R polar direction are less pronounced than the other Bi–B correlations, reinforcing the idea that Bi and Ti determine their own local polar displacements whereas those of Fe and Mg are driven by Bi. The presence of octahedral tilting in the present case results in different local symmetry from the off-axis A site displacements here than in the untilted⁴⁹ PZT monoclinic phases.

■ ASSOCIATED CONTENT

📄 Supporting Information

Transformation matrix relating rhombohedral and monoclinic cells, BVS values for refined configurations, correlation functions from BVS-only constrained RMC refinements, bond angle distributions, Bi–O pair correlations as a function of Ti neighbors, additional cation displacement analysis, and

representations of the local Bi environment. This material is available free of charge via the Internet at <http://pubs.acs.org>.

AUTHOR INFORMATION

Corresponding Author

J.B.Claridge@liverpool.ac.uk; M.J.Rosseinsky@liverpool.ac.uk

Notes

The authors declare no competing financial interest.

ACKNOWLEDGMENTS

We thank the Engineering and Physical Sciences Research Council (EPSRC) for funding under Grants EPSRC/CS11794 and EP/H000925/1. We acknowledge Prof. Alex C. Hannon for assistance with correction of the total scattering data and Dr. Andrew L. Goodwin for help in determining DCFs. We thank the STFC for access to the ISIS Facility.

REFERENCES

- (1) ShROUT, T. R.; ZHANG, S. J. *J. Electroceram.* **2007**, *19*, 111.
- (2) DAMJANOVIC, D.; KLEIN, N.; LI, J.; POROKHONSKYY, V. *Funct. Mater. Lett.* **2010**, *3*, 5.
- (3) SUGAWARA, F.; IIDA, S.; SYONO, Y.; AKIMOTO, S.-I. *J. Phys. Soc. Jpn.* **1965**, *20*, 1529.
- (4) TOMASHPOL'SKII, Y. Y.; VENEVTSEV, Y. N. *Inorg. Mater.* **1969**, *5*, 1087.
- (5) ISHIWATA, S.; AZUMA, M.; TAKANO, M.; NISHIBORI, E.; TAKATA, M.; SAKATA, M.; KATO, K. *J. Mater. Chem.* **2002**, *12*, 3733.
- (6) INAGUMA, Y.; KATSUMATA, T. *Ferroelectrics* **2003**, *286*, 111.
- (7) INAGUMA, Y.; MIYAGUCHI, A.; KATSUMATA, T. *Mater. Res. Soc. Symp. Proc.* **2003**, *755*, DD12.10.1.
- (8) AZUMA, M.; TAKATA, K.; SAITO, T.; ISHIWATA, S.; SHIMAKAWA, Y.; TAKANO, M. *J. Am. Chem. Soc.* **2005**, *127*, 8889.
- (9) BELIK, A. A.; LIKUBO, S.; KODAMA, K.; IGAWA, N.; SHAMOTO, S.-I.; NIITAKA, S.; AZUMA, M.; SHIMAKAWA, Y.; TAKANO, M.; IZUMI, F.; TAKAYAMA-MUROMACHI, E. *Chem. Mater.* **2006**, *18*, 798.
- (10) SUCHOMEL, M. R.; FOGG, A. M.; ALLIX, M.; NIU, H.; CLARIDGE, J. B.; ROSSEINSKY, M. J. *Chem. Mater.* **2006**, *18*, 4987.
- (11) KHALYAVIN, D. D.; SALAK, A. N.; VYSHATKO, N. P.; LOPES, A. B.; OLEKHNOVICH, N. M.; PUSHKAREV, A. V.; MAROZ, I. I.; RADYUSH, Y. V. *Chem. Mater.* **2006**, *18*, 5104.
- (12) SUCHOMEL, M. R.; THOMAS, C. I.; ALLIX, M.; ROSSEINSKY, M. J.; FOGG, A. M.; THOMAS, M. F. *Appl. Phys. Lett.* **2007**, *90*, No. 112909.
- (13) HUGHES, H.; ALLIX, M. M. B.; BRIDGES, C. A.; CLARIDGE, J. B.; KUANG, X.; NIU, H.; TAYLOR, S.; SONG, W.; ROSSEINSKY, M. J. *J. Am. Chem. Soc.* **2005**, *127*, 13790.
- (14) BRIDGES, C. A.; ALLIX, M.; SUCHOMEL, M. R.; KUANG, X.; STERIANOU, I.; SINCLAIR, D. C.; ROSSEINSKY, M. J. *Angew Chem., Int. Ed.* **2007**, *46*, 8785.
- (15) KUBEL, F.; SCHMID, H. *Acta Crystallogr., Sect. B* **1990**, *46*, 698.
- (16) EGAMI, T.; BILLINGE, S. J. L. *Underneath the Bragg Peaks: Structural Analysis of Complex Materials*; Pergamon: Oxford, U.K., 2003.
- (17) HANNON, A. C. In *Encyclopedia of Spectroscopy and Spectrometry*; LINDON, J.; TRANTER, G.; HOLMES, J., Eds.; Academic Press: London, 2000; Vol. 2, p 1493.
- (18) KEEN, D. J. *Appl. Crystallogr.* **2001**, *34*, 172.
- (19) KEEN, D. A.; TUCKER, M. G.; DOVE, M. T. *J. Phys.: Condens. Matter* **2005**, *17*, S15.
- (20) TUCKER, M. G.; KEEN, D. A.; DOVE, M. T.; GOODWIN, A. L.; HUI, Q. *J. Phys.: Condens. Matter* **2007**, *19*, No. 335218.
- (21) HUI, Q.; DOVE, M. T.; TUCKER, M. G.; REDFERN, S. A. T.; KEEN, D. A. *J. Phys.: Condens. Matter* **2007**, *19*, No. 335214.
- (22) HUI, Q.; TUCKER, M. G.; DOVE, M. T.; WELLS, S. A.; KEEN, D. A. *J. Phys.: Condens. Matter* **2005**, *17*, S111.
- (23) GOODWIN, A.; REDFERN, S.; DOVE, M.; KEEN, D.; TUCKER, M. *Phys. Rev. B* **2007**, *76*, No. 174114.
- (24) KRAYZMAN, V.; LEVIN, I.; WOICIK, J. C.; PROFFEN, T.; VANDERAH, T. A.; TUCKER, M. G. *J. Appl. Crystallogr.* **2009**, *42*, 867.
- (25) JEONG, I.; PARK, C. Y.; KIM, D. J.; KIM, S.-H.; MOON, B. K.; KIM, I. W.; AHN, C. W. *Z. Kristallogr.* **2011**, *226*, 150.
- (26) LIU, X.; ABRAHAMS, I.; HULL, S.; NORBERG, S. T.; HOLDYNSKI, M.; KROK, F. *Solid State Ionics* **2011**, *192*, 176.
- (27) NORBERG, S. T.; ERIKSSON, S. G.; HULL, S. *Solid State Ionics* **2011**, *192*, 409.
- (28) SHOEMAKER, D. P.; SESHADRI, R.; HECTOR, A. L.; LLOBET, A.; PROFFEN, T.; FENNIE, C. J. *Phys. Rev. B* **2010**, *81*, No. 144113.
- (29) NORBERG, S. T.; TUCKER, M. G.; HULL, S. *J. Appl. Crystallogr.* **2009**, *42*, 179.
- (30) SOPER, A. K.; BARNEY, E. R. *J. Appl. Crystallogr.* **2011**, *44*, 714.
- (31) HANNON, A. C.; HOWELLS, W. S.; SOPER, A. K. *ATLAS: Analysis of Time-of-Flight Diffraction Data from Liquid and Amorphous Samples*; Report RAL-89-046; Rutherford Appleton Laboratory: Didcot, U.K., 1989.
- (32) LARSON, A. C.; VON DREELE, R. B. *General Structure Analysis System (GSAS)*; Report LAUR 86-748; Los Alamos National Laboratory: Los Alamos, NM, 2004.
- (33) CORKER, D. L.; GLAZER, A. M.; WHATMORE, R. W.; STALLARD, A.; FAUTH, F. *J. Phys.: Condens. Matter* **1998**, *10*, 6251.
- (34) DOVE, M. T.; TUCKER, M. G.; KEEN, D. A. *Eur. J. Mineral.* **2002**, *14*, 331.
- (35) ABRAMOV, Y. A.; TSIRELSON, V. G.; ZAVODNIK, V. E.; IVANOV, S. A.; BROWN, I. D. *Acta Crystallogr., Sect. B* **1995**, *51*, 942.
- (36) KWEI, G. H.; LAWSON, A. C.; BILLINGE, S. J. L.; CHEONG, S. W. *J. Phys. Chem.* **1993**, *97*, 2368.
- (37) TUCKER, M. G. Unpublished data, 2010.
- (38) FRANTTI, J.; LAPPALAINEN, J.; ERIKSSON, S.; IVANOV, S.; LANTTO, V.; NISHIO, S.; KAKIHANA, M.; RUNDLÖF, H. *Ferroelectrics* **2001**, *261*, 193.
- (39) RAGINI; RANJAN, R.; MISHRA, S. K.; PANDEY, D. *J. Appl. Phys.* **2002**, *92*, 3266.
- (40) DMOWSKI, W.; EGAMI, T.; FARBER, L.; DAVIES, P. K. *AIP Conf. Proc.* **2001**, *582*, 33.
- (41) GRINBERG, I.; COOPER, V. R.; RAPPE, A. M. *Nature* **2002**, *419*, 909.
- (42) COOPER, V. R.; GRINBERG, I.; MARTIN, N. R.; RAPPE, A. M. *AIP Conf. Proc.* **2002**, *626*, 26.
- (43) NOHEDA, B.; COX, D.; SHIRANE, G. *Appl. Phys. Lett.* **1999**, *74*, 2059.
- (44) NOHEDA, B.; GONZALO, J. A.; CROSS, L. E.; GUO, R.; PARK, S. E.; COX, D. E.; SHIRANE, G. *Phys. Rev. B* **2000**, *61*, 8687.
- (45) KUNZ, M.; BROWN, I. D. *J. Solid State Chem.* **1995**, *115*, 395.
- (46) PANDEY, D.; SINGH, A. K.; BAIK, S. *Acta Crystallogr., Sect. A* **2007**, *64*, 192.
- (47) SCHÖNAU, K. A.; SCHMITT, L. A.; KNAPP, M.; FUESS, H.; EICHEL, R.-A.; KUNGL, H.; HOFFMANN, M. *J. Phys. Rev. B* **2007**, *75*, No. 184117.
- (48) FRANTTI, J. *J. Phys. Chem. B* **2008**, *112*, 6521.
- (49) PHELAN, D.; LONG, X.; XIE, Y.; YE, Z. G.; GLAZER, A.; YOKOTA, H.; THOMAS, P.; GEHRING, P. *Phys. Rev. Lett.* **2010**, *105*, No. 207601.